Appl. Phys. B 76, 277–284 (2003)
DOI: 10.1007/s00340-002-1088-0

Applied Physics B
Lasers and Optics

S. BOLLANTI[1,✉]
F. BONFIGLI[1]
E. BURATTINI[2]
P. DI LAZZARO[1]
F. FLORA[1]
A. GRILLI[2]
T. LETARDI[1]
N. LISI[1]
A. MARINAI[3]
L. MEZI[1]
D. MURRA[1]
C. ZHENG[4]

High-efficiency clean EUV plasma source at 10–30 nm, driven by a long-pulse-width excimer laser

[1] ENEA C.R. Frascati, P.O. Box 65, 00044 Frascati, Italy
[2] INFN-LNF, via Enrico Fermi 40, 00044 Frascati, Italy
[3] ENEA Guest, Italy
[4] El.En. S.p.A., via Baldanzese 17, 50041 Calenzano, Italy

Received: 21 October 2002
Published online: 26 February 2003 •

ABSTRACT A long-pulse-width high-output energy (120 ns FWHM, 7 J) XeCl laser has been focused on thin tape targets (Cu and Ta) to generate more than 100-ns-long (FWHM) EUV pulses in the 10–30 nm spectral region, suitable for projection microlithography. The conversion efficiency was more than 20% over a 2π solid angle. We observed debris emission using a gated CCD camera, and measured the debris speed for different irradiation conditions. We found irradiation conditions such that the measured velocities were low enough that simple mechanical devices combined with krypton at low-pressure could efficiently stop both ionic debris and cluster debris. Our results show that a suitable combination of driving-laser characteristics, target material and thickness, environment gas and mechanical choppers can make clean and increase the power of EUV solid-target laser-plasma sources.

PACS 52.50.J.m; 52.38.P.h; 81.16.N.d

1 Introduction

The recent realisation of high-reflectivity multilayer mirrors down to a wavelength of 11 nm [1–4] has provided much stimulus to the projection EUVL (Extreme UltraViolet Lithography) technique, the feasibility of which relies on the development of cheap, clean and reliable soft X-ray sources. Compared to expensive synchrotrons, laser-generated plasmas are cheap and powerful sources. One of the main problems for laser-plasma generated X-ray sources is the production of debris from the target, which is detrimental to soft X-ray optics. Several techniques have been considered for reducing this contamination, such as the use of very thin tape targets ($< 30\,\mu$m) irradiated with very short pulses ($\approx$ ps) [5], droplet liquid targets [6], gas jet targets [7], and cryogenic Xe targets [8, 9]. In all these cases, the target characteristics (small thickness and/or low density) require high laser irradiances ($I_L \approx 10^{12}$–10^{14} W/cm^2), thus reducing the soft X-ray conversion efficiency in the 100 eV spectral region. Moreover, in the case of non-solid targets, residual vapours in the vacuum chamber heavily absorb the emitted radiation, unless a more complex configuration is set up [10].

✉ Fax: +39-06/9400-5334, E-mail: bollanti@frascati.enea.it

Due to the high energy per pulse of our laser-driver, we were able to increase the laser spot size on the target from 30 μm (at best focusing) to more than 300 μm (by defocusing the beam). As a result, the laser irradiance was decreased to 10^{10} W/cm^2, thereby reducing the debris emission from a 30 μm-thick tape target. At this irradiance level the production efficiency of EUV photons was very high, since the EUV pulse duration was almost as long as that of the laser. Consequently, a high X-ray emission per pulse was achieved.

2 The laser-plasma source

Our soft X-ray laser-plasma source has been detailed elsewhere [11–15], so it will only be briefly outlined here. The driver is a XeCl ($\lambda = 308$ nm) excimer laser facility named Hercules, developed at the ENEA Frascati laboratories. In order to have a high quality beam, Hercules is equipped with an unstable resonator. Due to the large volume and to the long self-sustained discharge, the laser system can reliably deliver an energy of 7 J with a pulse duration of 120 ns (FWHM), up to a maximum repetition rate of 5 Hz [12, 15]. The Hercules beam can be focused by an f# = 3 triplet lens to a 30-μm-diameter spot (86% encircled energy), reaching a maximum irradiance of $I_L \approx 5 \times 10^{12}$ W/cm^2.

Corresponding to different applications, the soft X-ray emission was measured in three different spectral regions:

S_{70} : $40\,\text{eV} < h\nu < 70\,\text{eV}$
(near the values for projection microlithography);

S_{ww} : $300\,\text{eV} < h\nu < 500\,\text{eV}$
(for contact microscopy, ww is for water window);

S_{1k} : $0.8\,\text{keV} < h\nu < 1.6\,\text{keV}$
(for radiobiology and contact microlithography).

The bandwidths of the three investigated spectral regions were determined by the combination of filters and detectors used in each case. In particular, the S_{70} bandwidth (40–70 eV) was limited by the transmission window of the 1.6-μm-thick aluminium filter, which cut off photon energies lower than 40 eV. In some cases, for example, when using a Cu target, a Cu mirror at a 5° grazing angle was used in order to cut off plasma photon energies higher than a few hundred eV energy.

We can optimise the emission in the different spectral regions by adjusting the laser parameters and choosing the most appropriate target material. In particular, copper (Cu) and tantalum (Ta) targets have shown very high emission efficiencies in the S_{70} region.

Throughout this paper we will assume that the emission of Ta targets (when irradiated at 10^{10} W/cm^2) is almost flat in the spectral region 40–120 eV [16], so that the efficiency per unit wavelength measured in the S_{70} interval can be extrapolated to 92.5 eV (13.4 nm), which is the standard wavelength selected for projection lithography.

The measured temporal behaviour of the soft X-ray pulse in each of the three spectral regions is shown, together with the laser pulse, in Fig. 1, for a 100-μm-thick Cu target. The calculated soft X-ray pulse energies in these spectral ranges are also indicated. It is evident that the long laser pulse-width largely favours emission in the S_{70} spectral range. The number of S_{70} photons can be further increased by suppressing the emission of the harder X-rays: this can be realised by moving the target by a distance of 1–2 mm from the position of the focus, as shown in Fig. 2.

At about 2 mm away from the focus, $I_L \sim 10^{10}$ W/cm^2, and the conversion efficiency obtained for a Ta target reached

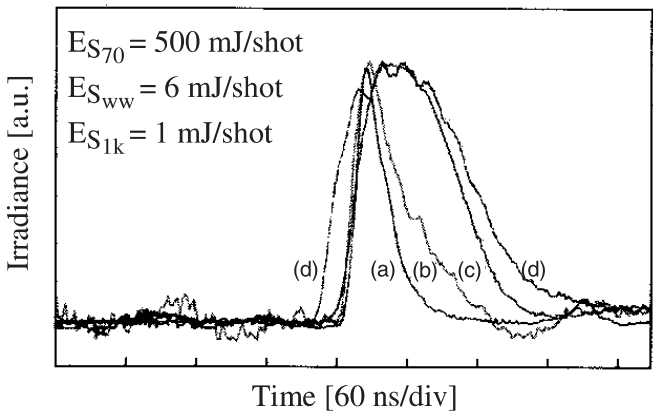

FIGURE 1 Time evolution of the 120-ns-long Hercules laser pulse (*curve d*) and of the soft X-rays in the S_{70}, S_{ww} and S_{1k} spectral regions (*curves c, b and a*, respectively). Laser irradiance $= 5 \times 10^{12}$ W/cm^2; target material: 100-μm-thick Cu tape (from [12])

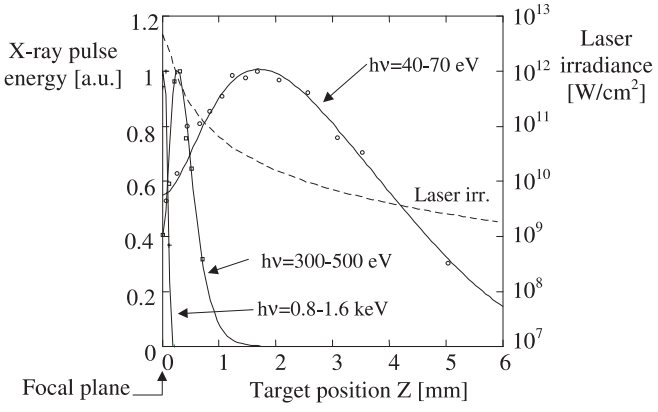

FIGURE 2 Soft X-ray pulse energy (in the S_{70}, S_{ww} and S_{1k} spectral intervals) and laser irradiance on the target (*dashed line*) vs. target position (behind the focal plane) for a 100-μm-thick Cu tape target irradiated by the 120 ns, 7 J Hercules laser pulse (from [15])

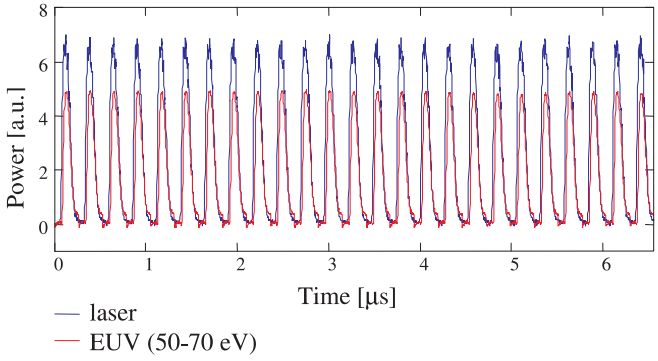

FIGURE 3 EUV pulse stability during a sequence of 25 laser shots on a Ta target at $I_L = 10^{10}$ W/cm^2 (out of focus). The time-gaps between shots have been eliminated. The laser pulse stability and the EUV pulse energy stability were 0.5 and 1% r.m.s., respectively

22% and 1 J of emitted X-rays in the S_{70} region. The corresponding spectral efficiency was 0.7%/eV over a 2π solid angle, which is very high compared with typical laser-plasma sources [17], and is larger by a factor of three than one of the best Xe vapour jet laser-plasma sources at 13.4 nm [10]. Under these conditions, the S_{70} EUV energy per pulse was also measured after reflection by a multilayer Mo/Si mirror (peak reflectivity $R = 30\%$, $\Delta\lambda/\lambda = 10\%$ around $\lambda = 18$ nm ≈ 70 eV, manufactured by the Lebedev Institute of Moscow [3]). A value of 10 mJ/shot/sr was obtained, in a good agreement with the 2π sr spectral efficiency of 0.7%/eV.

The EUV emission shot-to-shot stability when the target was out of focus was good, being less than 1% r.m.s., as shown in Fig. 3. This is due to the fact that for a defocused beam, the laser spot size is practically insensitive to target positioning instabilities.

3 Stopping debris

A severe problem with laser-plasma soft X-ray sources, when applied for example to EUV-lithography, is debris emission, which may limit the lifetime of the expensive relay optics that are placed close to the plasma source. This particulate emission is due to the compression of the liquid layer between the plasma and the solid target, and consists of debris particles with diameters ranging between less than 1 μm and ≈ 100 μm, with velocities up to several hundreds metres per second [18]. The use of non-solid targets can greatly reduce debris emission, but it also leads to a decrease in the X-ray production efficiency and in the set-up simplicity. For this reason we tried to exploit the characteristics of our source when working at low laser irradiance. In fact, when working out of focus, the laser irradiance decreases, causing the plasma pressure to drop and the debris to slow down [19]. Thus it is possible to use mechanical devices to stop the particles, in spite of the increase in average debris particle size $\bar{D} \propto \left(\varphi_L^4/\tau^2 P_0^2\right)^{1/3}$, where φ_L is the laser spot diameter, τ the laser pulse duration and P_0 the plasma pressure [18].

Preliminarily, we measured the debris speed at two different values of the laser irradiance. We used a gated CCD camera with an MCP intensifier (DiCAM II, PCO Computer Optics) to observe the visible debris ejected by a Ta target

at $I_L \sim 10^{10}$ and $\sim 3 \times 10^{12}$ W/cm^2. The results are shown in Fig. 4. In all cases, the exposure time was 1/10 of the delay between the laser pulse and the onset of the exposure, so that the length of the marks is 1/10 of the distance between the plasma source and the beginning of the mark. From Fig. 4c and d we can observe a strong reduction of the debris speed at $I_L \sim 10^{10}$ W/cm^2, which can be estimated to be about 100 m/s, in agreement with [18]. Another remarkable difference between higher and lower laser intensities is the debris angular distribution, being strongly peaked in the direction opposite to that of the laser in the first case, and rather isotropic in the second case.

The number of emitted debris particles also depended on the target material. In Fig. 5 debris emission under similar experimental conditions is measured both for yttrium (a) and tantalum (b,c), with the results for the last being three orders of magnitude lower than those for the first. The amount of visible cluster debris emitted by a 30-μm-thick Ta tape target placed out of focus was only 30 particle/sr per joule of laser pulse energy (see Fig. 5c). This figure is almost three orders of magnitude lower than the values reported in the literature [18], and is also lower than that for the target placed at best focusing (Fig. 5b). Clearly, not all the Ta debris fragments are visible in Fig. 4. The minimum size of visible debris particles depends on their speed, temperature and other parameters [15, 20]. For the images in Fig. 4 we calculated a minimum size $\varphi \approx 1$–2 μm, depending on the debris speed and the selected CCD gain. A detailed calculation of the minimum size of visible debris particles is given in the Appendix, and more data can be found in [20].

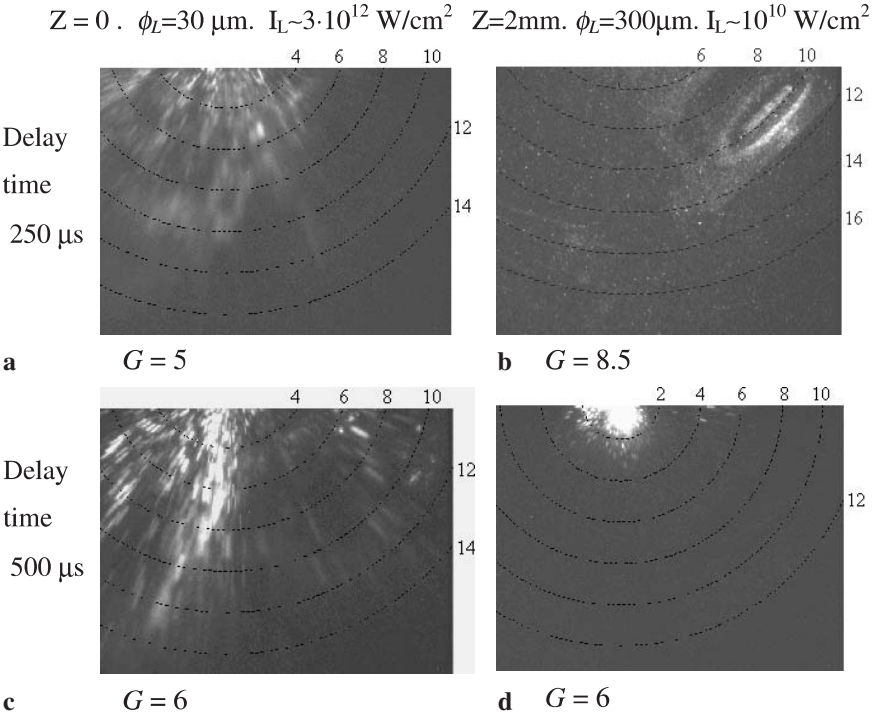

FIGURE 4 Debris emitted by a Ta target placed at the focal plane ($Z = 0$) and at $Z = +2$ mm after the focal plane, here observed by a gated intensified CCD at different delay values from the plasma formation. Laser parameters: 120 ns, 4 J. Laser incident angle: 45° from right hand. Vacuum pressure $< 10^{-3}$ mbar. *Dashed lines*: distance from the target (cm). $G = 1$–10 is the CCD gain

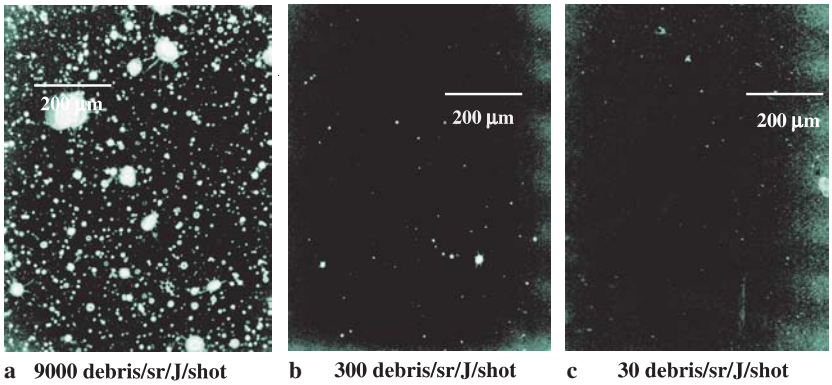

a 9000 debris/sr/J/shot (~ like in literature)
b 300 debris/sr/J/shot
c 30 debris/sr/J/shot

Yttrium target
450 shots in 1 bar He
Φ_L=30 μm
I_L~3·10^{12} W/cm^2

Tantalum target
600 shots in 1 bar He
Φ_L=30 μm
I_L~3·10^{12} W/cm^2

Tantalum target
500 shots in vacuum
Φ_L=450 μm
I_L~10^{10} W/cm^2

FIGURE 5 Debris emitted by different targets at different laser irradiance values, and collected on a plastic film. The images are negative and the films were observed using an optical microscope in transmission mode. The laser pulse energy was 4 J with a 120 ns pulse-width and the incident angle on the target was 45°. The plastic film was placed 5 cm away the target at 55° to the laser direction (where the maximum debris emission was)

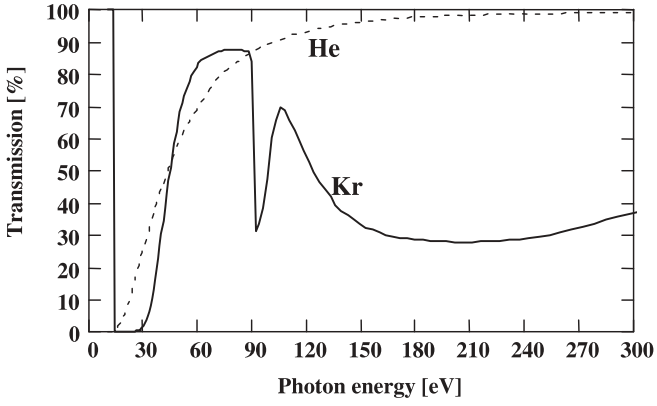

FIGURE 6 Transmission of Kr and He at 1 mbar over a length of 10 cm vs. the photon energy according to the data of Henke et al. [23]

The low debris speed obtained at $I_L \sim 10^{10}$ W/cm^2 makes it possible to stop most of the debris using a suitable combination of mechanical devices (for larger and slower particles), and Kr gas (for sub-micron debris and for ions). Obviously, the Kr gas pressure should be low enough to transmit the 60–90 eV EUV spectrum [21, 22]. Note that in this spectral region, Kr is more transparent than He [23] (the typical gas used for debris stopping), as shown in Fig. 6. Having a mass that is 21 times larger, it is also much more efficient in stopping both ionic debris as well as cluster debris, as shown in Fig. 7 [21, 22].

The use of Kr to stop debris was proposed few years ago [24], but the use of pure Kr (without choppers) is not enough for complete debris stopping, as demonstrated in the following.

We first tested a pure mechanical stopper (without Kr) made up of two counter-rotating disks (diameter $D_{\text{disk}} = 20$ cm), each with two holes ($D_{\text{hole}} = 2.5$ cm) on opposite sides of the disk near the edge. Their turning speeds were $\omega_1 = 75$ rps and $\omega_2 = 65$ rps, giving an "open" window of ≈ 0.3 ms and a "dark" window of ≈ 50 ms. A schematic is shown in Fig. 8. The first disk was 16 cm from the plasma. Only debris faster than $0.16 \times (3 \times 10^{-4})^{-1}$ m/s $= 530$ m/s could pass through the choppers.

We irradiated both a 30-μm-thick Ta tape and a 150-μm-thick magnesium (Mg) tape at low laser irradiance ($\sim 10^{10}$ W/cm^2), measuring the debris densities both on a plastic film behind the choppers and on another film as a reference, which was put beside the first chopper hole. The incident angle of the laser and the debris collection direction were at $+45°$ and $-45°$ with respect to the target normal, re-

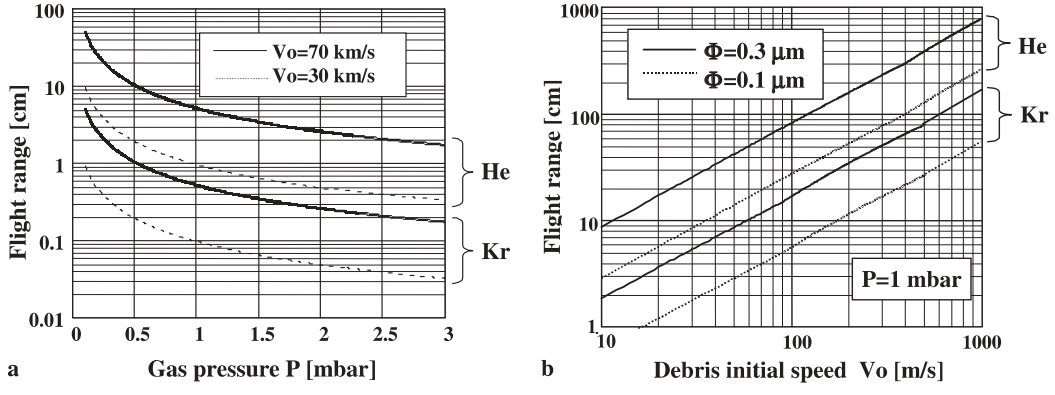

FIGURE 7 Calculated flight range of Ta ions **(a)** and debris **(b)** in He and in Kr vs. the gas pressure P and vs. the initial speed V_0. (φ = spherical debris diameter)

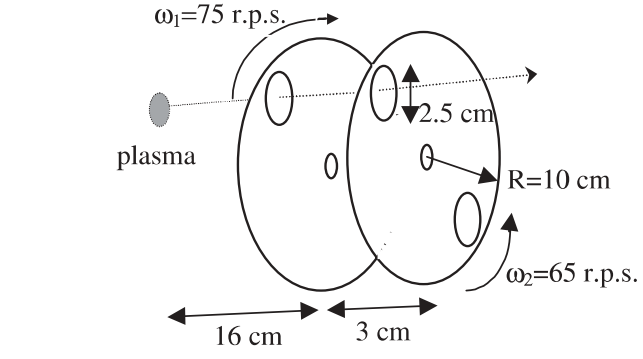

$$T_{open} = \frac{1}{\pi \cdot (\omega_1 + \omega_2)} \cdot \frac{D_{hole}}{D_{disk}} = 0.3\,\text{ms}$$

$$T_{closed} = \frac{1}{(\omega_1 - \omega_2)} = 50\,\text{ms}$$

FIGURE 8 Experimental set-up of the mechanical stopper based on the action of two counter-rotating choppers

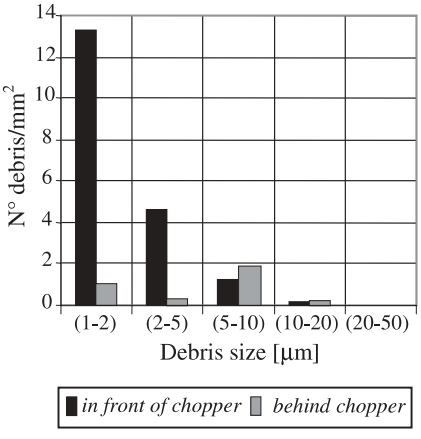

FIGURE 9 Debris density vs. debris particle size on plastic films put before (at 15 cm) and after the choppers. Target: 150 μ m-thick Mg irradiated by 10^3 shots at $I_L = 10^{10}$ W/cm^2 (see text). The data have been normalised with respect to the different distances from the plasma of the two films

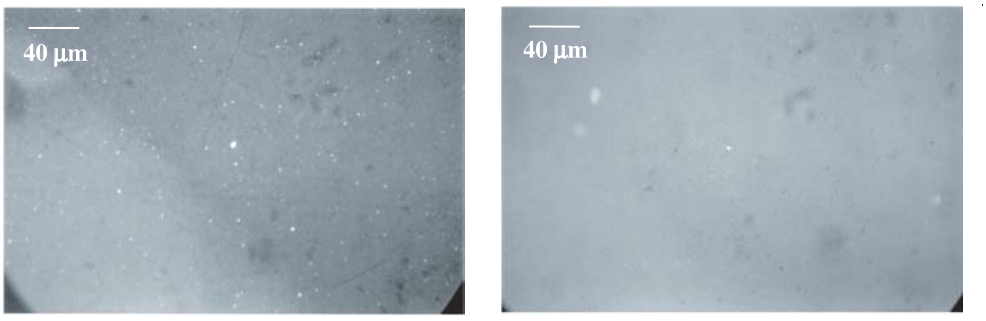

FIGURE 10 Debris deposited by 400 shots on a plastic film placed 4 cm from the 70-μm-thick Ta target in vacuum **(a)** and in Kr at 2.5 mbar **(b)**. The images were obtained using an optical microscope (objective 40×) in reflection mode. Laser parameters: 4 J, 120 ns, 10^{10} W/cm^2, 45° incident angle

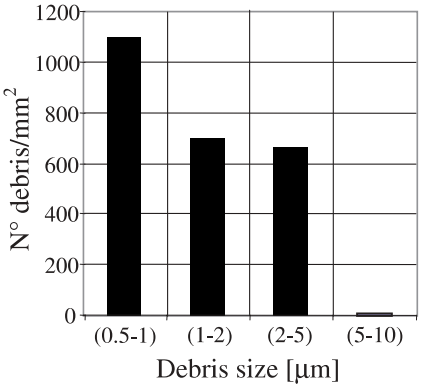

FIGURE 11 Debris density vs. debris particle size on plastic films measured from Fig. 10a. In the case of Fig. 10b, the debris density (∼ 1 particle/mm^2) is too low to plot a histogram

spectively. For both Mg and Ta targets the choppers reduced the total number of cluster debris particles ($\varphi > 0.5$ μm) by a factor 5 (from 30 particles/shot/sr/J, shown in Fig. 5c, down to 6 particles/shot/sr/J in the case of the Ta target). In the case of Mg, the number of debris particles was so high (about 10 times larger than that for Ta) that a size histogram of the debris could be obtained, as shown in Fig. 9. The reduction by a factor of 5 is much smaller than that expected from the debris velocity characterisation obtained from Fig. 4. This might be due to the distance used between the two disks of the chopper being too large (3 cm) in this experiment.

We also measured the capability of pure Kr (without choppers) to stop debris (both ionic and clusters). We placed a plastic film at 4 cm on the normal to a 70-μm-thick Ta target irradiated at $I_L \sim 10^{10}$ W/cm^2 and compared the debris deposition in vacuum and in Kr at 2.5 mbar, which transmits more than 80% of the EUV photons in the range 60–90 eV across the 4 cm gap. Figure 10 shows a noticeable capability of Kr to stop small-sized debris: in fact, the number of small debris particles deposited on the film was lower by more than two orders of magnitude in Kr than in vacuum. This ratio was obtained by counting the debris particles using the IDL 5.3 software (Research Systems, Inc.). The quantitative results are summarised in Fig. 11.

By comparing the histogram of the debris density in Fig. 11 with the debris density measured for the thinner Ta tape used during the choppers experiment (taking into account the different distances of the plastic films from the source), it turns out that the 70-μm-thick Ta tape target ejected about two order of magnitude more debris than the 30-μm-thick one at $I_L \approx 10^{10}$ W/cm^2. This is in agreement with the results reported in [25], where the comparison was made between solid and 60-μm-thick steel targets irradiated at $I_L \approx 10^{13}$ W/cm^2.

When using the low pressure Kr, the cluster debris mitigation factor is in good agreement with that expected from the theoretical debris range of flight (Fig. 7b). However, the factor of 70 reduction of ionic debris, estimated by comparing the optical densities of the films in Fig. 10a and b, is significantly smaller than that predicted on the basis of the range of flight of the ions (Fig. 7a): after 4 cm of flight in Kr at 2.5 mbar, practically no Ta ions (or neutrals) should be observed. A similar result is obtained when using a copper tape (100 μm thick) as the target, as shown in Fig. 12. In this case the ionic de-

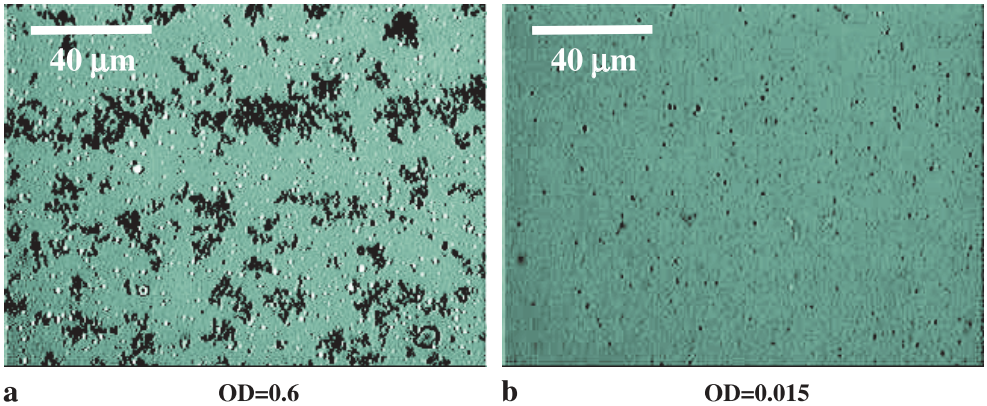

FIGURE 12 Debris deposited by 500 shots on a glass plate placed 4 cm from a 100-μm-thick Cu target in vacuum **(a)** and in Kr at 2.5 mbar **(b)**. The images were obtained using an optical microscope (objective 40×) in reflection mode. Laser parameters: 4 J, 120 ns, $I_L \sim 10^{10}$ W/cm^2, 45° incident angle. The optical densities of the two plates after the irradiation by 500 shots were $OD = 0.6$ and $OD = 1.5 \times 10^{-2}$, respectively

FIGURE 13 Copper layer spot deposited on a glass plate placed 6.5 cm from the plasma after being exposed to 1000 laser shots at $I_L = 10^{10}$ W/cm^2 on the Cu target using the Debris Mitigation System (DMS). The first chopper disk was 2 cm from the plasma and the Kr pressure was 2.5 mbar. The glass optical density on the spot, compared with a non-exposed glass, was $OD = 1.7 \times 10^{-3}$

bris emission was reduced by only a factor of 40 (estimated again on the basis of the optical density of the film), while the cluster debris emission was reduced by more than 2 orders of magnitude.

These experimental results can be explained by considering the momentum given by the Ta or Cu ions to the Kr gas: this momentum (measured to be 2×10^{-5} kg m s^{-1} sr^{-1} by using a ballistic pendulum placed in front of the copper tape) is high enough to push the Kr gas at high speed (up to 100 m/s at 4 cm from the target, quickly decreasing for larger distances) so that the Ta- (or Cu-)rich Kr cloud can condense over any surface it impinges upon while travelling. In this moving dirty cloud the Ta (Cu) ions are at rest with respect to Kr, not really contradicting the theoretical results of Fig. 7a.

A strong reduction of both the ionic and the cluster debris can be obtained only by using the Kr gas together with the choppers. In fact, the Ta (or Cu) cluster debris, slowed down by Kr, can be easily stopped by the choppers, while the ions are at first collected into the Kr dirty cloud, which is finally stopped by the choppers. In conclusion, the combined action of the two stopping techniques is much more effective than the product of the single mitigation factors.

A preliminary experiment to check the capability of this combined technique (Debris Mitigation System, DMS) was carried out using a Cu target. By placing the first chopper at just 2 cm from the Cu target and filling the chamber with 2.5 mbar of Kr, no cluster debris could be observed in the 0.2 sr collection angle, while the total mass density of ionic debris was reduced by more than a factor of 250, as shown in Fig. 13. Here the factor of 250 was obtained by comparing the optical densities of Figs. 12a and 13. For each case, the optical density was normalised both to the distance from the target and to the number of shots. This ENEA DMS, which is based on a combination of Kr gas and choppers, is now patent pending [26].

4 Concluding remarks

We have obtained a high laser-to-EUV conversion efficiency by using a high-energy, 120-ns-FWHM long optical pulse, emitted by the ENEA XeCl excimer laser facility Hercules and focused on solid tape targets. Operation at a low laser irradiance (out of focus) can optimise the EUV radiation production efficiency and reduce both the number and speed of debris particles. In the case of a Ta target, normalising data to the laser energy, we obtained an EUV emission of ≈ 0.5 mJ/shot/J/sr with a 1% bandwidth around 18 nm, together with a flux of 30 particle/shot/J/sr (debris particle size > 0.5 μm), as seen in Fig. 5. This debris flux was almost 3 orders of magnitude lower than a typical flux emitted by a solid-target plasma source [18]. We achieved a further reduction of the number of cluster debris particles by a factor of ~ 5 using a double mechanical chopper, which can stop debris with velocities lower than 530 m/s (see Fig. 9). An additional decrease of debris particle number by more than two orders of magnitude was realized using 2.5 mbar of Kr as a buffer gas. The ions and sub-micron debris were reduced by more than one order of magnitude by only using low-pressure Kr buffer gas (see Figs. 10, 11, 12) and by more than two orders of magnitude with the DMS (which combines the Kr buffer gas and mechanical choppers). The effectiveness of the DMS on the cluster debris was so high that it did not allow experimental measurement of the final mitigation factor, since our laser system is limited to a few thousand shots per day. For cluster debris, the combined action of mechanical choppers and Kr gas is also expected to overcome the product of the single effects, leading to a debris density lower than 10^{-2} particle/shot/J/sr.

In summary, we obtained an efficient and clean EUV laser plasma source by a suitable combination of the following experimental conditions: 1) a low irradiance level ($I_L \approx 10^{10}$ W/cm^2), which reduces the number of emitted debris particles; 2) a sufficiently thin tape target made of a convenient, low-debris-emission material; 3) two mechanical choppers, which stop slower debris particles regardless of their size; 4) low pressure Kr gas, which slows down debris and ions, significantly enhancing the effect of the choppers.

As a consequence, a long lifetime (defined as the number of shots causing a 10% decrease in the reflectivity) is expected for an EUV multilayer mirror placed 15 cm from the target in such a set-up, namely: a) $\sim 10^6$ shots J limited by the effect of small size ($\varphi < 0.5$ μm) and ionic debris; and b) 10^{11} shots J limited by the effect of large size debris ($\varphi > 0.5$ μm). These numbers can be obtained: a) from the optical density of 1.7×10^{-6}/shot at (6.5 cm, 4 J) of the deposited layer in Fig. 13, measured by a visible-light microdensitometer; this value has been scaled to the equivalent value at 90 eV [23, 27], also taking into account the double passage of EUV light upon reflection; b) from the experimental cluster debris density of 6 particle/shot/J/sr (see Figs. 5c and 9) reduced by the 2.5 mbar Kr mitigation factor ($> 10^2$, see Fig. 10). Experimental tests on mirror lifetime are planned for the near future. A further improvement is expected by flowing the Kr gas toward the target, in a purifying closed loop.

We also plan to develop a tape-like cryogenic target [28], which should further and significantly decrease the amount of debris. This type of target is different from those proposed in the past [8, 9]: it is made of a 100–300 μm solid layer of Kr or Xe that is continuously refreshed [28]. It is very similar to a tape target and is compatible with the excimer laser

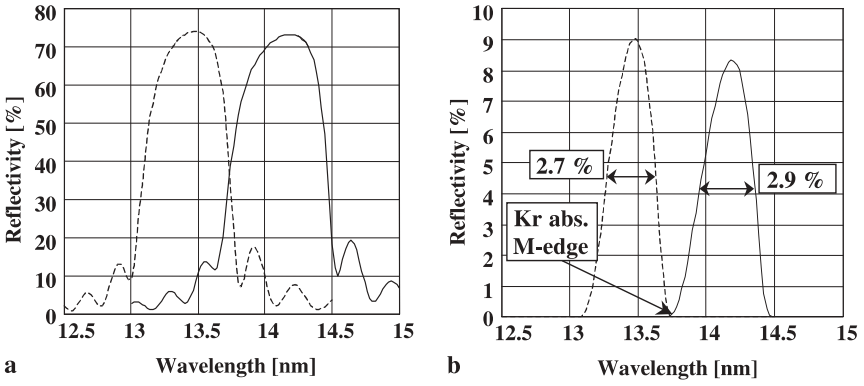

FIGURE 14 Theoretical reflectivity of Mo/Si multilayer mirrors optimised for 13.4 nm (92.5 eV, *dashed line*) and for 14.2 nm (88 eV, *solid line*), according to the data of Henke et al. [23, 31], obtained for a Mo-Si period of 6.9 and 7.3 nm, respectively, for one reflection **(a)** and for 8 consecutive reflections **(b)**. In **b** the FWHM bandwidths and the wavelength of the krypton absorption M-edge are also indicated

heating and with the Debris Mitigation System proposed here. Both the Kr and Xe materials are lighter than Ta, so a higher efficiency of the DMS is expected. In fact, in this case the cluster debris flying through the Kr gas would not only be slowed down but also evaporated, while the ionic debris would mix with the Kr gas rather than generating an aerosol-like dirty cloud. By using such a target it could be possible to approach the very long lifetime (10^{11} shots, i.e. 1 year at 5 kHz) required for EUVL system mirrors.

Finally, let us discuss two potential problems of the DMS proposed in this paper: 1) the choppers described above may seriously limit the collection solid angle of EUV radiation, but their angular speed in the present experiment is so modest that both the disk velocity as well as the disk holes diameter can be significantly increased; 2) in order to use the Kr-based DMS for EUVL, it is necessary to shift the operating wavelength for projection lithography from the standard value of 13.4 nm [8, 10, 29, 30] to 14.2 nm, since the 13.4 nm wavelength is in the poor transmission region of Kr (see Fig. 6, $\lambda = 13.4$ nm corresponding to $h\nu = 92.5$ eV). This shift is not a serious problem, since when the wavelength is increased, the smaller peak reflectivity of Mo/Si multilayer mirrors is fully compensated by their larger bandwidth, as experimentally demonstrated in [4] and as shown in Fig. 14. On the other hand, the high absorption of Kr far away from $\lambda = 14.2$ nm is very useful for limiting the mirror heating by out-of-band radiation absorption.

Appendix

The time behaviour of the Ta debris temperature $T(t)$, for different debris particle diameter values, can be estimated assuming that they are emitted at the Ta boiling temperature, T_0, and that, while travelling in the vacuum, their temperature cools down just because of black-body irradiation. Neglecting room temperature, we have

$$T(t) = \sqrt[3]{\frac{T_0^3}{1 + 18 T_0^3 \xi \frac{\sigma t}{C_s \varrho D}}}, \tag{A.1}$$

where $T_0 = 5698$ K = tantalum boiling temperature, $\xi \sim 0.4$ = Ta total normal emissivity (neglecting its T-dependence), $C_s = 200$ J/kg/°C = Ta specific heat, $\varrho = 16\,600$ kg/m^3 = Ta density, σ = Stefan-Boltzmann constant, and D = debris diameter value.

When debris particles reach the melting temperature T_m, they stay at this temperature during the melting/solidification time t_m, given by

$$t_{\mathrm{m}} = \frac{\varrho \cdot C_{\mathrm{m}}}{6 \cdot \xi \cdot \sigma} \frac{D}{T_{\mathrm{m}}^4}, \tag{A.2}$$

where $T_m = 3269$ K = melting temperature, and $C_m = 173$ kJ/kg = melting specific heat.

Then, debris continues to cool down following (A.1). The resulting temperature behaviour is shown in Fig. 15.

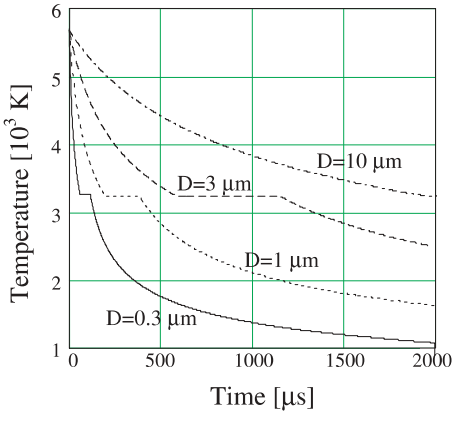

FIGURE 15 Tantalum debris temperature vs. time for different debris particle sizes (see (A.1) and (A.2))

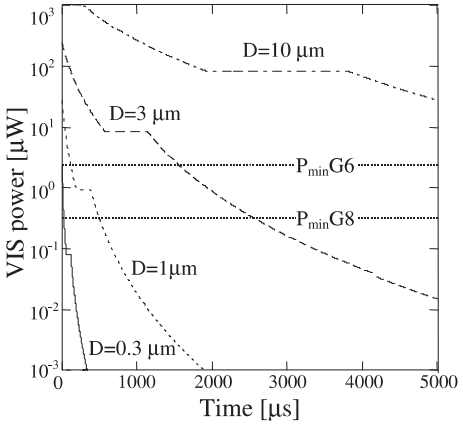

FIGURE 16 Time-behaviour of power emitted by Ta debris within a 4π sr in the visible range, for different debris sizes (see (A.3)). The minimum power levels P_{min} detectable by the CCD camera with gains of $G = 6$ and $G = 8$ (as given by (A.4)) are shown for reference

Figure 16 shows the power irradiated by the debris in the visible range, calculated as

$$P(t) = \xi \cdot \pi \cdot D^2 \cdot \sigma \cdot T^4 \frac{\int_{400\text{nm}}^{700\text{nm}} BB(T,\lambda)}{\int_{0}^{\infty} BB(T,\lambda)}, \quad \text{(A.3)}$$

where $BB =$ black body spectrum. In the same figure, this power is compared with the minimum power, P_{min}, required to detect the debris using the CCD camera:

$$P_{\min} = F_{\min} \frac{(V_\mathrm{d} \cdot I)\, \Phi_\mathrm{im}}{T_\mathrm{lens}} \frac{4\pi}{\Omega}, \quad \text{(A.4)}$$

where $F_{\min} = N_{\min} \dfrac{h\nu}{\left(L_\mathrm{pix}\right)^2} \mathrm{e}^{G_\mathrm{max}-G}$, $N_{min} = 30 =$ minimum photons/pixel detectable by the CCD at the maximum MCP gain G_max, $L_\mathrm{pix} = 20\,\mu\mathrm{m} =$ pixel size, $G = 6$ and $G = 8$ are the selected MCP gain factors, $V_\mathrm{d} = 100\,\mathrm{m/s}$ (for example, estimated from Fig. 4d) = debris speed, $I = 1/15 =$ CCD objective demagnification factor, $\Phi_\mathrm{im} = 60\,\mu\mathrm{m} =$ debris image size (constant due to the objective aberrations), $h\nu = 2\,\mathrm{eV} =$ photon energy, $\Omega = 3.4 \times 10^{-3}\,\mathrm{sr} =$ objective collected solid angle, $G_\mathrm{max} = 10 =$ maximum MCP gain of the CCD, and $T_\mathrm{lens} = 0.8 =$ objective transmission factor.

Figure 16 shows that after a time-window of 500 μs, like in the cases of Fig. 4c and d, only debris larger than 1 μm still emit sufficient power to be detected.

ACKNOWLEDGEMENTS The authors would like to thank the group led by Prof. A. Reale in the Physics Department of L'Aquila University for its contribution to the experiments.

REFERENCES

1 C. Montcalm, S. Bajt, P.B. Mirkarimi, E.A. Spiller, F.J. Weber, J.A. Folta: Proc. SPIE **3331**, 42 (1998)
2 J.H. Underwood: Proc. SPIE **2523**, 51 (1995)
3 I.A. Artyukov, A.I. Fedorenko, V.V. Kondratenko, S.A. Yulin, A.V. Vinogradov: Opt. Commun. **102**, 401 (1993)
4 S. Bajt, J.B. Alameda, T.W. Barbee, W.M. Clift, J.A. Folta, B.B. Kaufmann, E.A. Spiller: Proc. SPIE **4506**, 65 (2001)
5 H. Shields, M.F. Powers, I.C.E. Turcu, I.N. Ross, J.R. Maldonado, P.G. Burkhalter, D.A. Newman: Proc. SPIE **2523**, 122 (1995)
6 H.M. Hertz, L. Rymell, M. Berglund, L. Malmqvist: Proc. SPIE **2523**, 88 (1995)
7 H. Fiedorowicz, A. Bartnik, R. Jarocki, M. Szczurek, T. Wilhein: Appl. Phys. B **67**, 391 (1998)
8 P. Celliers, L.B. DaSilva, C.B. Dane, S. Mrowka, M. Norton, J. Harder, L. Hackel, D.L. Matthews, H. Fiedorowicz, A. Bartnik, J.R. Maldonado, J.A. Abate: J. Appl. Phys. **79**, 8258 (1996)
9 H.M. Hertz, M. Berglund, B.A. Hansson, L. Rymell: Proc. SPIE **3767**, 2 (1999)
10 G.D. Kubiak, L.J. Bernardez, K.D. Krenz, W.C. Replogle, W.C. Sweatt, D.W. Sweeney, R.M. Hudyma, H. Shields: Proc. SPIE **3767**, 136 (1999)
11 S. Bollanti, R. Cotton, P. Di Lazzaro, F. Flora, T. Letardi, N. Lisi, D. Batani, A. Conti, L. Palladino, A. Reale, M. Belli, F. Ianzini, A. Scafati, L. Reale, A. Tabocchini, A. Faenov, T. Pikuz, A. Osterheld: Nuovo Cimento D **18**, 1241 (1996)
12 S. Bollanti, P. Albertano, M. Belli, P. Di Lazzaro, A.Y. Faenov, F. Flora, G. Giordano, A. Grilli, F. Ianzini, S.V. Kukhlevsky, T. Letardi, A. Nottola, L. Palladino, T. Pikuz, A. Reale, L. Reale, A. Scafati, M.A. Tabocchini, I.C.E. Turcu, K. Vigli-Papadaki, G. Schina: Nuovo Cimento D **20**, 1685 (1998)
13 S. Bollanti, P. Di Lazzaro, F. Flora, G. Giordano, T. Letardi, G. Schina, C.E. Zheng, L. Filippi, L. Palladino, A. Reale, G. Taglieri, D. Batani, A. Mauri, M. Belli, A. Scafati, L. Reale, P. Albertano, A. Grilli, A. Faenov, T.A. Pikuz, R. Cotton: J. X-ray Sci. Technol. **5**, 261 (1995)
14 S. Bollanti, R.A. Cotton, P. Di Lazzaro, F. Flora, T. Letardi, N. Lisi, D. Batani, A. Conti, A. Mauri, L. Palladino, A. Reale, A.Y. Faenov, T.A. Pikuz, A.L. Osterheld: Proc. SPIE **2523**, 70 (1995)
15 S. Bollanti, P. Di Lazzaro, F. Flora, T. Letardi, A. Marinai, A. Nottola, K. Vigli-Papadaki, A. Vitali, F. Bonfigli, N. Lisi, L. Palladino, A. Reale, C.E. Zheng: Proc. SPIE **3767**, 33 (2000)
16 G.M. Zeng, H. Daido, T. Nishikawa, H. Takabe, S. Nakayama, H. Aritome, K. Murai, Y. Kato, M. Nakatsuka, S. Nakai: J. Appl. Phys. **75**, 1923 (1994); see also F. Bijkerk, A.P. Shevelko, L.A. Shmaenok, S.S. Churilov: Proc. SPIE **3157**, 236 (1997)
17 W.T. Silfvast: IEEE J. Quantum Electron. **35**, 700 (1999)
18 H.A. Bender, D. O'Connell, W.T. Silfvast: Appl. Opt. **34**, 6513 (1995)
19 V.G. Bakaev, V.Yu. Korol', I.G. Lebo, N.N. Mel'nik, G.E. Metreveli, A.G. Molchanov, V.V. Nikishin, V.B. Rozanov, G.V. Sychuqov, V.F. Tishkin, V.D. Zvorykin: 'Laser-Target Interactions in KrF GARPUN Facility'. In: *Reprint No 69 of Lebedev Physical Inst.*, (Russian Academy of Sciences, Moscow 1997)
20 S. Bollanti, P. Di Lazzaro, F. Flora, L. Mezi, D. Murra, C. Zheng: Eur. Phys. J. D (2002) submitted
21 T. Letardi, D. Lo, C. Zheng: J. Appl. Phys. **89**, 1458 (2001)
22 F. Flora, L. Mezi, C.E. Zheng F. Bonfigli: Europhys. Lett. **56**, 676 (2001)
23 B.L. Henke, E.M. Gullikson J.C. Davis: At. Data Nucl. Data Tables **54**, 181 (1993)
24 F. Bijkerk, L. Shmaenok, A. Vanhonk, R. Bastiaensen, Y.Y. Platonov, A.P. Shevelko, A.V. Mitrofanov, F. Voss, R. Desor, H. Frowein, B. Nikolaus: J. Phys. III **4**, 1669 (1994)
25 I.C.E. Turcu, J.B. Dance: *X-Rays From Laser Plasmas – Generation and Applications*, (Wiley, New York 1999), p. 222
26 F. Flora, L. Mezi, C. Zheng: Italian Patent No. RM2000 A000636 (2000)
27 M.A. Ordal, L.L. Long, R.J. Bell, S.E. Bell, R.R. Bell, R.W. Alexander Jr., C.A. Ward: Appl. Opt. **22**, 1099 (1983)
28 T. Mochizuki, A. Shimoura, S. Amano, S. Miyamoto: Proc. SPIE **4504**, 87 (2001)
29 D. Attwood: *Soft X-rays and Extreme Ultraviolet Radiation: Principles and Applications*, (Cambridge University Press, Cambridge 1999)
30 R.H. Stulen, D.W. Sweeney: IEEE J. Quantum Electron. **35**, 694 (1999)
31 Web site: http://cindy.lbl.gov/optical_constants